PNAS RESEARCH ARTICLE | MICROBIOLOGY OPEN ACCESS

Evidence of antigenic drift in the fusion machinery core of SARS-CoV-2 spike

Timothy J. C. Tan[a], Abhishek K. Verma[b], Abby Odle[b], Ruipeng Lei[c], David K. Meyerholz[d], Kenneth A. Matreyek[e], Stanley Perlman[b,f], Lok-Yin Roy Wong[b,g,h,1], and Nicholas C. Wu[a,c,i,j,1]

Edited by Peter Palese, Icahn School of Medicine at Mount Sinai, New York, NY; received October 4, 2023; accepted February 23, 2024

Antigenic drift of SARS-CoV-2 is typically defined by mutations in the N-terminal domain and receptor binding domain of spike protein. In contrast, whether antigenic drift occurs in the S2 domain remains largely elusive. Here, we perform a deep mutational scanning experiment to identify S2 mutations that affect binding of SARS-CoV-2 spike to three S2 apex public antibodies. Our results indicate that spatially diverse mutations, including D950N and Q954H, which are observed in Delta and Omicron variants, respectively, weaken the binding of spike to these antibodies. Although S2 apex antibodies are known to be nonneutralizing, we show that they confer protection in vivo through Fc-mediated effector functions. Overall, this study indicates that the S2 domain of SARS-CoV-2 spike can undergo antigenic drift, which represents a potential challenge for the development of more universal coronavirus vaccines.

SARS-CoV-2 | antibody | deep mutational scanning | spike | S2 domain

Significance

The rapid emergence of naturally circulating SARS-CoV-2 variants poses a significant challenge to the development of long-lasting, effective vaccines and therapeutics. Mutations in the spike protein of SARS-CoV-2 can lead to successful escape from protective antibodies, and hence antigenic drift. Most of these spike mutations are known to occur in the receptor binding domain and N-terminal domain. In contrast, while human antibodies also target the conserved S2 domain, whether S2 mutations also contribute to SARS-CoV-2 antigenic drift remains largely elusive. This study used a high-throughput approach to identify S2 mutations that weaken binding to a multidonor class of S2 antibodies. Our findings have significant implications for SARS-CoV-2 evolution as well as the development of more universal coronavirus vaccines.

As the major antigen of severe acute respiratory syndrome coronavirus 2 (SARS-CoV-2), the spike (S) glycoprotein has undergone extensive antigenic drift since the beginning of the COVID-19 pandemic (1). SARS-CoV-2 S protein is a homotrimer with an N-terminal domain (NTD), a receptor-binding domain (RBD), and an S2 domain. S protein facilitates virus entry by engaging the host receptor angiotensin-converting enzyme II (ACE2) via RBD and mediating virus–host membrane fusion through the fusion machinery in S2 (2). While all three domains in S can elicit antibody responses during infection or vaccination, the neutralizing potency of antibodies to RBD and NTD are typically much higher than those to S2 (3). Consistently, mutations in RBD and NTD are key determinants of SARS-CoV-2 antigenic drift (1, 4, 5). Although mutations in S2 have also emerged in circulating SARS-CoV-2 variants (1), they are thought to mainly affect the stability and fusogenicity of S protein (6–8). As a result, whether S2 mutations play a role in the antigenic drift of SARS-CoV-2 remains largely elusive.

Due to the relatively high sequence conservation of S2, human antibodies to S2 can achieve exceptional breadth. For example, human antibodies to the S2 fusion peptide can neutralize coronavirus strains from different genera (α, β, γ, and δ) (9–12). Besides, human antibodies to the S2 stem helix can neutralize diverse β-coronavirus strains (13–17). Additionally, a public clonotype to the apex of S2 can cross-react with multiple sarbecoviruses (18, 19). This public clonotype is encoded by IGHV1-69/IGKV3-11 with complementarity determining region (CDR) H3 and L3 lengths of 15 and 11 amino acids (IMGT numbering), respectively (18, 19). Although S2 antibodies usually have weak neutralizing activity, antibodies to fusion peptide and stem helix have been shown to confer in vivo protection against SARS-CoV-2 infection (9–17). Given that S2 antibodies are commonly observed in both vaccinated and infected individuals (20, 21), they may exert selection pressure on the circulating SARS-CoV-2.

In this study, we showed that the IGHV1-69/IGKV3-11 public clonotype to the apex of S2 confers partial in vivo protection through Fc-mediated effector functions, despite their lack of neutralizing activity (18). Subsequently, a deep mutational scanning experiment was performed to probe the effects of S2 mutations on the cell-surface binding activity of three IGHV1-69/IGKV3-11 S2 antibodies, namely COVA1-07, COVA2-14, and COVA2-18. Specifically, we focused on single amino acid mutations within the first heptad repeat (HR1) and central helix (CH). Our results revealed that D950N and Q954H, which are observed in Delta and Omicron variants, respectively (1), weakened binding of SARS-CoV-2 S to all three IGHV1-69/IGKV3-11 S2 antibodies. Collectively, these results indicate that S2 mutations contribute to SARS-CoV-2 antigenic drift.

Author contributions: T.J.C.T., L.-Y.R.W., and N.C.W. designed research; T.J.C.T., A.K.V., A.O., R.L., D.K.M., and L.-Y.R.W. performed research; K.A.M., S.P., and L.-Y.R.W. contributed new reagents/analytic tools; T.J.C.T., L.-Y.R.W., and N.C.W. analyzed data; and T.J.C.T., L.-Y.R.W., and N.C.W. wrote the paper.

Competing interest statement: N.C.W. serves as a consultant for HeliXon. All authors declare no other competing interests.

This article is a PNAS Direct Submission.

[1]To whom correspondence may be addressed. Email: roy.wong@rutgers.edu or nicwu@illinois.edu.

This article contains supporting information online at https://www.pnas.org/lookup/suppl/doi:10.1073/pnas.2317222121/-/DCSupplemental.

Published April 1, 2024.

Results

In Vivo Protection Activity of IGHV1-69/IGKV3-11 S2 Antibodies. Previous studies have reported a public clonotype against the S2 domain that is encoded by IGHV1-69/IGKV3-11 (18, 19). Here, we tested the in vivo protection activity of three previously identified IGHV1-69/IGKV3-11 S2 antibodies, namely COVA1-07, COVA2-14, and COVA2-18 (18). Based on survival analysis (Fig. 1*A*) and weight loss profiles (Fig. 1*B*), all three antibodies showed prophylactic protection in vivo against a lethal challenge of SARS2-N501Y$_{MA30}$, which is a mouse-adapted strain of SARS-CoV-2 (22). BALB/c mice treated with COVA1-07 showed 60% survival, while those with COVA2-14 and COVA2-18 showed 80% survival. In contrast, all mice treated with CR9114, which is an influenza virus-specific antibody (23), succumbed to infection. This result indicates that although IGHV1-69/IGKV3-11 S2 antibodies have no neutralizing activity (18), they contribute to protective antibody responses against severe SARS-CoV-2 infection. Since COVA2-18 showed the highest weight recovery out of all three S2 antibodies tested (Fig. 1*B*), it was selected as a representative IGHV1-69/IGKV3-11 S2 antibody for further characterization. Histopathological analysis showed that pulmonary edema was more extensive in mice treated with control antibody CR9114 than those treated with COVA2-18 (Fig. 1 *C* and *D*). Besides, mice treated with COVA2-18 had approximately ten-fold lower viral titer than those treated with CR9114 at 4 d postinfection (Fig. 1*E*). To elucidate the mechanism of in vivo protection, we prophylactically treated mice with COVA2-18 WT or COVA2-18 with the L234A, L235A, and P329G mutations (COVA2-18 LALA-PG) to abolish its Fc effector function (24). Upon challenge with SARS2-N501Y$_{MA30}$, mice treated with COVA2-18 LALA-PG showed 0% survival, whereas all mice treated with WT COVA2-18 survived (Fig. 1 *F* and *G*). These data demonstrate that the in vivo protective activity of IGHV1-69/IGKV3-11 S2 antibodies is mainly due to Fc-mediated effector functions. Similarly, a previous

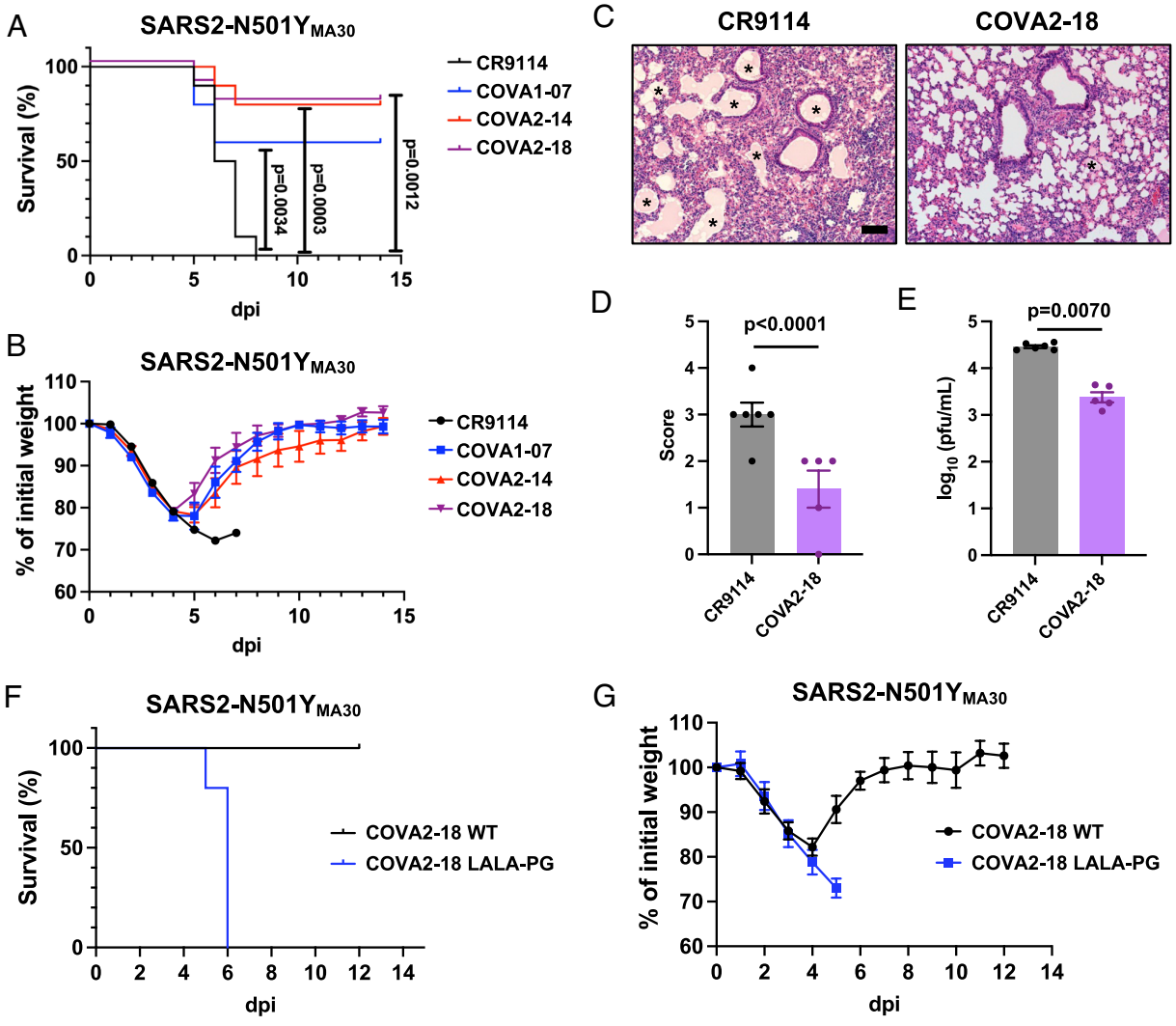

Fig. 1. In vivo protection activity of IGHV1-69/IGKV3-11 S2 antibodies. (*A* and *B*) BALB/c mice were intravenously injected with 200 μg of CR9114 (black), COVA1-07 (blue), COVA2-14 (red), or COVA2-18 (purple) 16 h before intranasal infection with 5,000 PFU of SARS2-N501Y$_{MA30}$, which is a nonrecombinant mouse-adapted strain of SARS-CoV-2 (22). Of note, nonrecombinant SARS2-N501Y$_{MA30}$ was used in this experiment. (*A*) Kaplan–Meier survival curves, and (*B*) weight loss profiles are shown (n = 10 per group). The log-rank test was used to calculate p-values in Kaplan–Meier survival curves. Weight loss profiles are shown as mean ± SEM. (*C*) Representative lung sections, stained with hematoxylin and eosin, from mice treated with control antibody CR9114 or COVA2-18. Pulmonary edema (*) was more extensive in lungs of the control group than COVA2-18-treated group. (Scale bar: 113 μm.) (*D*) Pulmonary edema was scored (n = 6 for the CR9114 group, n = 5 for the COVA2-18 group). Bar plots show mean ± SEM, with individual data points shown. Two-way Student's t-test was performed. (*E*) Viral lung titers were measured from lungs of CR9114- or COVA2-18-treated BALB/c mice 4 d postinfection (n = 6 for the CR9114 group, n = 5 for the COVA2-18 group). Bar plots show mean ± SEM, with individual data points shown. Two-way Student's t-test was performed. (*F* and *G*) BALB/c mice were intravenously injected with 200 μg of COVA2-18 WT (black) or COVA2-18 LALA-PG (blue) antibody 16 h before intranasal infection with 5,000 PFU of SARS2-N501Y$_{MA30}$. (*F*) Kaplan–Meier survival curves, and (*G*) weight loss profiles are shown (n = 5 per group). Weight loss profiles are shown as mean ± SEM.

study has reported that COV2-2164, which is another member of the IGHV1-69/IGKV3-11 public clonotype to S2, modestly reduces the viral load in the lung and brain of K18-hACE2 transgenic mice upon SARS-CoV-2 infection, albeit with no effect on weight loss (19).

Deep Mutational Scanning of S2 against IGHV1-69/IGKV3-11 Antibodies. Given that IGHV1-69/IGKV3-11 S2 antibodies exhibited in vivo protection activity, we were interested in whether mutations in S2 could influence their binding activity. To systematically identify mutations on the S protein that affect binding to IGHV1-69/IGKV3-11 S2 antibodies, we performed a deep mutational scanning (DMS) experiment using our previously constructed S mutant library, which contained all possible amino acid mutations from residues 883 to 1034, spanning HR1 and CH in the S2 domain (25). Briefly, this mutant library was displayed on human embryonic kidney 293T (HEK293T) landing pad cells. Fluorescence-activated cell sorting (FACS) was then performed to sort individual mutants according to their cell-surface binding activity to COVA1-07, COVA2-14, and COVA2-18 (*SI Appendix*, Fig. S1). Occurrence frequency of each mutant in different sorted populations was quantified by next-generation sequencing. For each experiment, a binding score was computed for each of the 1931 missense mutations, 122 silent mutations, and 132 nonsense mutations. The binding score was normalized such that the average score of silent mutations was 1 and that of nonsense mutations was 0.

Our DMS experiments were highly reproducible, with a Pearson correlation coefficient of 0.90 to 0.92 between independent biological replicates (*SI Appendix*, Fig. S2 *A–C*). In addition, the binding score distributions of nonsense and silent mutations had minimal overlap, indicating that our DMS experiments could distinguish mutants with different cell-surface binding activities to COVA1-07, COVA2-14, and COVA2-18 (*SI Appendix*, Fig. S2 *D–F*). We also observed a high Pearson correlation coefficient of 0.97 among the DMS experiments against COVA1-07, COVA2-14, and COVA2-18 (*SI Appendix*, Fig. S2 *G–I*), indicating that the same mutation would have a similar effect on cell-surface binding activity against these three antibodies. This result was not unexpected given that COVA1-07, COVA2-14, and COVA2-18 belong to the same IGHV1-69/IGKV3-11 public clonotype (18).

Two Natural S2 Mutations Weaken Binding to IGHV1-69/IGKV3-11 Antibodies. To investigate whether the binding activity of IGHV1-69/IGKV3-11 S2 antibodies could be affected by S2 mutations, we aimed to identify S2 mutations that weakened the binding activity to COVA1-07, COVA2-14, and COVA2-18. Since our deep mutational scanning experiments relied on cell surface display, mutations that lowered the cell-surface expression level would result in a lower binding score even if it did not affect the antibody binding affinity. Therefore, we compared the binding scores of individual mutations to their cell-surface expression levels which were previously quantified using the RBD antibody CC12.3 (25, 26). As expected, there was a mild correlation between the binding score and expression score, which is a proxy for the cell-surface expression level (25) (Pearson correlation coefficient of 0.48 to 0.49, Fig. 2). Nevertheless, there were mutations with high expression scores but low binding scores, such as T961F, V987C, Q1005R, and Q1010W, all of which rarely occurred in circulating SARS-CoV-2 (27). Similarly, the low binding scores of D950N and Q954H, which are fixed in Delta and Omicron variants, respectively (1), did not seem to be explained by the expression score alone. As a result, the low binding scores of these mutations were likely due to their effects on the antibody binding affinity, rather than cell-surface expression level.

To experimentally validate our findings, S protein bearing S2 mutations D950N, Q954H, T961F, V987C, Q1005R, and Q1010W were individually expressed by transient transfection of HEK293T cells, which were subsequently analyzed by flow cytometry using COVA1-07, COVA2-14, COVA2-18, and CC12.3 (*SI Appendix*, Fig. S3). Compared to wild type (WT), these six mutations have lower cell-surface binding activity to COVA1-07, COVA2-14, and COVA2-18, albeit to different extents (Fig. 3 *A* and *C*). T961F, Q1005R, and Q1010W weakened the cell-surface binding activity of these three antibodies by >80%, whereas D950N, Q954H, and V987C only weakened their binding activity by ~40%, ~25%, and ~50%, respectively. In contrast, their cell-surface binding activity to the RBD antibody CC12.3 was similar to or higher than WT (Fig. 3*D*). In this validation experiment, we also included mutation V915H as a control, which had a binding score of >3 against COVA1-07, COVA2-14, and COVA2-18 in our deep mutational scanning experiments, but a WT-like expression score (Figs. 2 and 3 *A–D*). These results

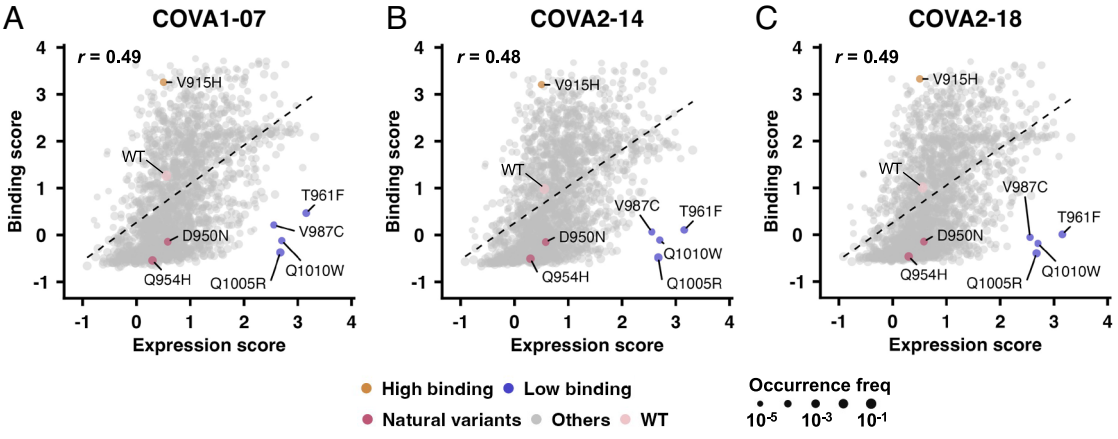

Fig. 2. Identification and validation of public S2 HR1/CH antibody escape mutations. Plots of binding scores to (*A*) COVA1-07, (*B*) COVA2-14, and (*C*) COVA2-18 against expression scores. One datapoint represents one amino acid mutation in our mutant library. One high binding, four low binding, and two natural mutations that were selected for subsequent validation experiments are colored in orange, purple, and red, respectively. Expression scores were obtained from our previous study (25). Pearson's correlation coefficient is shown. Occurrence frequency of each mutant is the average frequency across six experiments (*Methods*). All data points are sized according to their occurrence frequency. Biological replicates of expression and binding sorting experiments were performed starting from the sorting step on the same library (*Methods*).

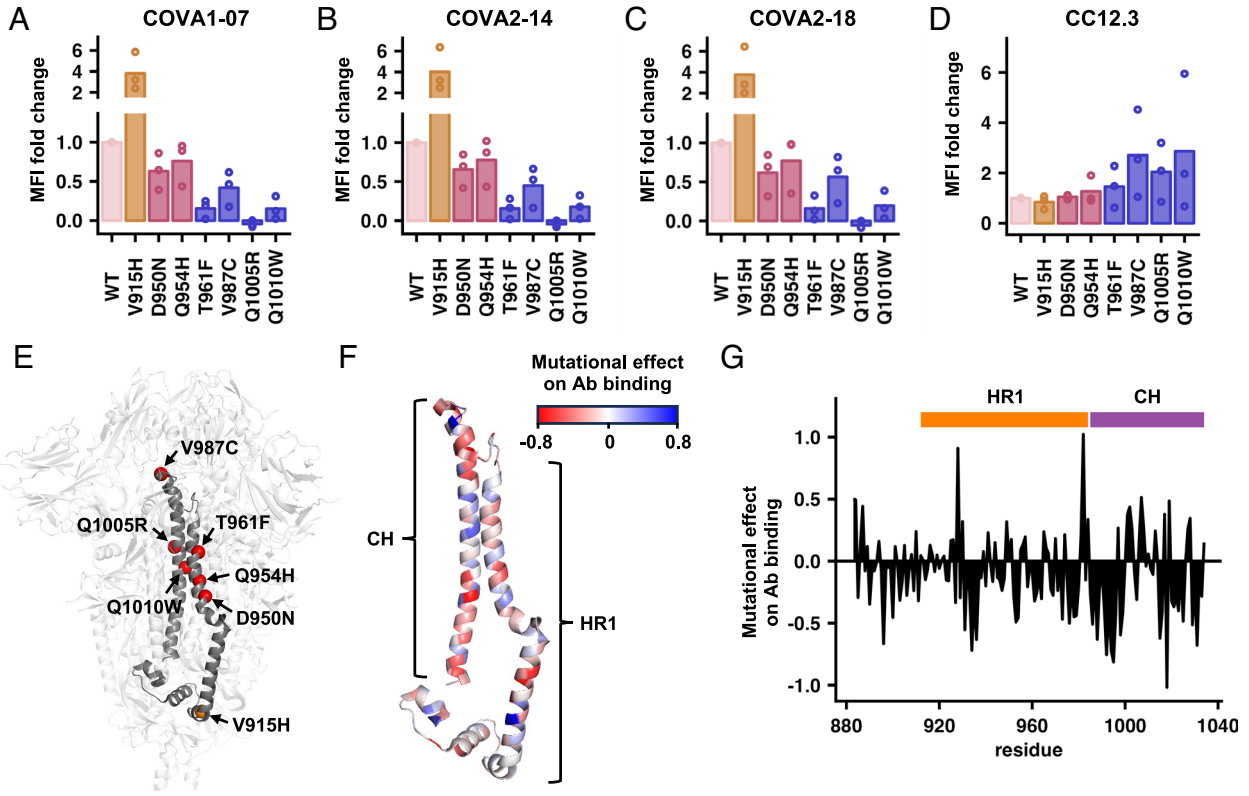

Fig. 3. Experimental validation of mutations that influence binding to IGHV1-69/IGKV3-11 S2 antibodies. (*A*–*D*) The binding of individual mutants to (*A*) COVA1-07, (*B*) COVA2-14, (*C*) COVA2-18, and (*D*) CC12.3 was individually analyzed using flow cytometry. For each mutant, fold change of median fluorescence intensity (MFI) compared to the WT is shown (*Methods*). (*E*) The locations of D950N, Q954H, T961F, V987C, Q1005R, and Q1010W are highlighted as red spheres on one protomer of the SARS-CoV-2 S structure (PDB 6VXX) (28). The location of V915H is highlighted as an orange sphere. Our mutant library contained mutations from residues 883 to 1,034, which are in gray on one protomer. Three independent biological replicates were performed. (*F*) Mutational effect on antibody binding is shown on the SARS-CoV-2 S structure (PDB 6VXX) (28). Only residues 883 to 1,034 of one protomer are shown. (*G*) Mutational effect on antibody binding is plotted against the residue position. CH: central helix; HR1: first heptad repeat.

indicate that D950N, Q954H, T961F, V987C, Q1005R, and Q1010W can weaken the binding activity of IGHV1-69/IGKV3-11 S2 antibodies. Moreover, since D950N and Q954H can be observed in the natural variants of SARS-CoV-2 (1), our results also suggest that antigenic drift occurs in the S2 domain.

We further analyzed the antibody binding effects of mutations found in recent Omicron lineages using our DMS binding data. BA.1, BA.2.75, XBB.1.5, BA.2.86, and JN.1 contain the Q954H and N969K mutations. While the Q954H mutation weakened binding to public IGHV1-69/IGKV3-11 antibodies (Figs. 2 and 3), the N969K mutation did not affect binding to these antibodies (*SI Appendix*, Fig. S4). S939F found in BA.2.86 and JN.1 slightly reduced binding to these antibodies, whereas L981F did not affect binding to IGHV1-69/IGKV3-11 public antibodies (*SI Appendix*, Fig. S4). Of note, the measurements for N969K and L981F might be noisy since their occurrence frequency was below our cutoff (*Methods*).

Spatially Diverse S2 Residues Modulate Binding to IGHV1-69/IGKV3-11 Antibodies. S2 mutations that were validated to influence the binding activity of IGHV1-69/IGKV3-11 antibodies were spatially distributed widely (Fig. 3*E*). For example, V987C, which decreased the binding to IGHV1-69/IGKV3-11 antibodies, resided at the S2 apex. In contrast, V915H, which increased the binding to IGHV1-69/IGKV3-11 antibodies, was at the bottom of the S2 domain. Other experimentally validated mutations, namely D950N, Q954H, T961F, Q1005R, and Q1010W, were located at the center of the S2 domain.

We further performed a systematic analysis using our deep mutational scanning data. To correct for the effect of S expression level on cell-surface binding activity, we computed an adjusted binding score, which represented the residual of a linear regression model of binding score on expression score. Subsequently, for a given S2 residue, the mutational effect on antibody binding was computed as the average adjusted binding score for all mutations at that residue (*Methods*). A positive mutational effect on antibody binding indicated that mutations tended to increase binding to IGHV1-69/IGKV3-11 antibodies, whereas negative indicated that mutations tended to decrease binding. Consistent with diverse spatial distribution of the validated mutations, residues with strong mutational effects on antibody binding, either positive or negative, were spread across the S2 domain (Fig. 3 *F* and *G*). Similarly, a previous study has shown that the binding activity of COV2-2164 and CnC2t1p1 B10, which belong to the same IGHV1-69/IGKV3-11 clonotype as COVA1-07, COVA2-14, and COVA2-18, can be abolished by spatially distinct mutations in the S2 (K814A, I980A, R995A, and Q1002A) (19). Therefore, the binding activity of IGHV1-69/IGKV3-11 antibodies can be modulated by S2 mutations that are outside of the epitope.

Since the epitope of these IGHV1-69/IGKV3-11 antibodies is exposed only when the S protein is in open conformations (18), any mutations that alter the conformational dynamics of the S protein may affect the binding to IGHV1-69/IGKV3-11 antibodies. For example, HexaPro, which consists of six proline mutations to stabilize the prefusion conformation, was previously shown to dramatically decrease the on-rate of the

IGHV1-69/IGKV3-11 antibodies (18). Consistently, S2 mutations T961F and Q1005R, which were validated to weaken the binding to IGHV1-69/IGKV3-11 antibodies (Fig. 3 *A*–*D*), were previously shown to be fusion-incompetent (25). Previous studies also hinted that the natural mutations D950N and Q954H altered the conformational dynamics of the S protein (29, 30)—D950N was shown to slightly promote membrane fusion (29), whereas Q954H was shown to favor a kinked conformation of HR1 (30). These observations could explain the diverse spatial distribution of S2 residues that influence binding to IGHV1-69/IGKV3-11 antibodies.

Discussion

Public antibodies against viral antigens such as influenza hemagglutinin, HIV envelope protein, and SARS-CoV-2 S have been documented (31–33). Since these antibodies are found in many individuals, public antibodies can exert a positive selection pressure on virus at the population level, which in turn promote antigenic drift. For example, natural mutations K417N/T in the S of many SARS-CoV-2 variants abrogate binding to public RBD antibodies encoded by IGHV3-53/3-66 (34–36). Our study here suggests a similar phenomenon in the relatively conserved core fusion machinery of SARS-CoV-2 S protein. Specifically, we show that natural S2 mutations D950N and Q954H can weaken the binding to public antibodies encoded by IGHV1-69/IGKV3-11. Our results further suggest that the in vivo protection activity of these IGHV1-69/IGKV3-11 antibodies can be affected by natural S2 mutations. Therefore, while neutralizing antibodies are known to exert positive selection pressure on SARS-CoV-2 (1, 4, 5), nonneutralizing antibodies that are protective, such as IGHV1-69/IGKV3-11 S2 antibodies (18), may do the same but to a lesser extent. Other traits not tested in this study, including innate immune evasion due to entry pathway preference (37) as well as spike protein folding dynamics (38, 39), could also select for these mutations that reduce binding with these protective, nonneutralizing S2 antibodies.

A previous study has shown that the binding of IGHV1-69/IGKV3-11 antibodies to the S2 apex requires an open conformation of the S protein (18). These observations imply that the epitope of IGHV1-69/IGKV3-11 S2 antibodies is exposed for binding when the S protein is transitioning from prefusion to postfusion conformations. If the epitope is only available during an intermediate state between prefusion and postfusion conformations of the S protein, any mutations that decrease the half-life of such an intermediate state will weaken the binding to IGHV1-69/IGKV3-11 S2 antibodies. These mutations can either stabilize the prefusion conformation to prevent transition to the intermediate state or accelerate the transition from the intermediate state toward the postfusion conformation. Consistently, mutations that weaken the binding to IGHV1-69/IGKV3-11 S2 antibodies include those that abolish fusion activity (e.g., T961F and Q1005R) (25) and enhance fusion activity (e.g., D950N) (29). Nevertheless, the conformation dynamics of S protein during the fusion process remains largely elusive. In addition, a high-resolution structure of an IGHV1-69/IGKV3-11 S2 antibody in complex with S2 is lacking. These limitations prevent a detailed mechanistic understanding of mutations that weaken the binding to IGHV1-69/IGKV3-11 S2 antibodies.

As SARS-CoV-2 continues to evolve in the human population and other coronavirus strains remain a pandemic threat, there is an urge to develop a more universal coronavirus vaccine (40). Its feasibility is substantiated by the discovery of broadly protective antibodies to the highly conserved S2 domain (9–17). However, our results suggest that escape mutations against S2 antibodies can emerge in naturally circulating SARS-CoV-2 variants. A previous study has shown that S2 mutation D796H, which locates near the base of the S protein and emerged in a chronically infected patient, reduces sensitivity to neutralization by convalescent plasma (41). More recently, a deep mutational scanning study of the full SARS-CoV-2 S protein has also identified natural mutations that can escape antibodies to the S2 stem helix (42). Consequently, potential escape mutations may impose a challenge for S2-based vaccine development (43–45).

Methods

Cell Culture. Human embryonic kidney 293T (HEK293T) cells (ATCC) were grown and maintained at 37 °C, 5% CO_2, and 95% humidity in D10 medium: Dulbecco's modified Eagle medium (DMEM) with high glucose (Gibco) supplemented with 10% v/v fetal bovine serum (FBS; Gibco), 1× nonessential amino acids (Gibco), 1× GlutaMAX (Gibco), 100 U/mL penicillin and 100 μg/mL streptomycin (Gibco). HEK293T landing pad cells were grown and maintained in D10 medium supplemented with 2 μg/mL doxycycline (Thermo Scientific) at 37 °C, 5% CO_2, and 95% humidity. Expi293F suspension cells (Gibco) were grown and maintained in Expi293 expression medium (Gibco) at 37 °C, 125 rpm, 8% CO_2, and 95% humidity according to the manufacturer's instructions.

Plasmid Construction. The S2 HR1/CH mutant library was constructed in our previous study (25). For experimental validation, codon-optimized oligonucleotide encoding S (GenBank: MN908947.3) with the PRRA motif in the furin cleavage site deleted was cloned into a phCMV3 vector. Site-directed mutagenesis was performed using PrimeSTAR Max DNA polymerase (Takara Bio) with the following settings: 98 °C for 10 s, 22 cycles of (98 °C for 10 s, 55 °C for 5 s, 72 °C for 45 s), 72 °C for 45 s. The PCR product was digested with DpnI (NEB) for 2 h at 37 °C and transformed into chemically competent DH5α *Escherichia coli*.

Antibody Expression and Purification. The heavy and light chain sequences of COVA1-07, COVA2-14, COVA2-18, CC12.3, and CR9114 were synthesized commercially (Integrated DNA Technologies), amplified via PCR, and cloned into a phCMV3 vector in an IgG1 format with a murine immunoglobulin kappa secretion signal sequence. The L234A, L235A, and P329G mutations were used to generate COVA2-18 IgG with the LALA-PG mutations in the constant region of the heavy chain. Plasmids encoding heavy and light chains were transfected into Expi293F cells in a 2:1 mass ratio using an ExpiFectamine 293 transfection kit (Gibco). Six days posttransfection, the supernatant was harvested via centrifugation of cell suspension at 4 °C and 4,500 × *g* for 30 min. The supernatant was clarified using a polyethersulfone membrane filter with a 0.22 μm pore size (Millipore).

CaptureSelect CH1-XL beads (Thermo Scientific) were washed thrice with MilliQ H_2O and resuspended in 1× PBS. The clarified supernatant was incubated with washed beads at 4 °C overnight with gentle rocking. Flowthrough was subsequently collected, and beads washed once with 1× PBS. Beads were incubated in 60 mM sodium acetate, pH 3.7 for 10 min at 4 °C for elution of the antibodies. Antibodies were further purified by size-exclusion chromatography using a Superdex 200 XK 16/100 column in 1× PBS. Fractions corresponding to ~150 kDa were pooled and concentrated using a centrifugal filter unit with a 30 kDa molecular weight cutoff (Millipore) via centrifugation at 4,000 × *g* and 4 °C for 15 min. Antibodies were stored at 4 °C.

Fluorescence-Activated Cell Sorting. HEK293T landing pad cells expressing the S2 HR1/CH mutant library of S as constructed previously (25) were harvested and centrifuged at 300 × *g* for 5 min at 4 °C. Supernatant was discarded. Cells were resuspended in ice-cold FACS buffer. Cells were incubated with 3 μg/mL of COVA1-07, 3 μg/mL of COVA2-14, or 10 μg/mL of COVA2-18 for 1 h at 4 °C with gentle rocking. Subsequently, cells were washed once, and resuspended with ice-cold FACS buffer. Cells were incubated with 2 μg/mL of PE anti-human IgG Fc. Cells were washed once, resuspended in ice-cold FACS buffer, and filtered through a 40 μm strainer. Cells were sorted via a three-way sort using a BigFoot spectral cell sorter (Invitrogen) according to levels of PE fluorescence at 4 °C. Cells with no PE fluorescence were sorted into "bin 0." Cells with PE at similar levels as WT were sorted into "bin 1." Cells with PE at higher levels than WT were sorted into "bin 2." Gating strategy is shown in *SI Appendix*, Fig. S1. Cells collected per bin for each replicate and antibody are listed in *SI Appendix*, Table S1. Biological

replicates of expression and binding sorting experiments were performed starting from the sorting step on the same library.

Postsorting Genomic DNA Extraction. Cell pellets were obtained via centrifugation at 300 × *g* for 15 min at 4 °C, and the supernatant was discarded. Genomic DNA was extracted using a DNeasy Blood and Tissue Kit (Qiagen) following the manufacturer's protocols with a modification, where resuspended cells were lysed at 56 °C for 30 min instead of 10 min.

Next-Generation Sequencing. After genomic DNA extraction, the region of interest spanning the HR1 and CH was amplified via PCR using 5′-CAC TCT TTC CCT ACA CGA CGC TCT TCC GAT CTA CAT CTG CCC TGC TGG CCG GCA CA-3′ and 5′-GAC TGG AGT TCA GAC GTG TGC TCT TCC GAT CTG CAA AAG TCC ACT CTC TTG CTC TG-3′ as forward and reverse primers, respectively. A maximum of 500 ng of genomic DNA was used as template per reaction. In total, a maximum of 4 μg per bin per replicate was used as template (i.e., eight reactions). PCR was performed using KOD DNA polymerase (Takara Bio) with the following settings: 95 °C for 2 min, 25 cycles of (95 °C for 20 s, 56 °C for 15 s, 68 °C for 20 s), 68 °C for 2 min, 12 °C hold. After PCR, all eight 50 μL reactions per bin per replicate were mixed. Then, 100 μL of product per bin per replicate was used for purification using a PureLink PCR Purification kit (Invitrogen). Subsequently, 10 ng of the purified PCR product per bin per replicate was appended with Illumina barcodes via PCR using primers: 5′-AAT GAT ACG GCG ACC ACC GAG ATC TAC ACX XXX XXX XAC ACT CTT TCC CTA CAC GAC GCT-3′, and 5′-CAA GCA GAA GAC GGC ATA CGA GAT XXX XXX XXG TGA CTG GAG TTC AGA CGT GTG CT-3′. Positions annotated by an "X" represented the nucleotides for the index sequence. This PCR was performed using KOD DNA polymerase with the following settings: 95 °C for 2 min, 9 cycles of (95 °C for 25 s, 56 °C for 15 s, 68 °C for 20 s), 68 °C for 2 min, 12 °C hold. Barcoded products were mixed and sequenced with a MiSeq PE300 v3 flow cell (Illumina).

Analysis of Next-Generation Sequencing Data. Forward and reverse reads were merged using PEAR (46). Forward reads were translated and matched to the corresponding mutant. Counts for each bin for each replicate were tabulated. A pseudocount of 1 was added to all counts. For each replicate, the frequency of each mutant was calculated as the count of that mutant, C_{mut}, divided by the total number of counts in that bin:

$$F_{mut,binX} = \frac{C_{mut,binX}}{\Sigma C_{binX}} \text{for } X = 0, 1, 2.$$

Cell count per mutant per replicate was calculated as follows:

$$T_{mut} = \sum_{x=0}^{2} F_{mut,binX} \times \text{cell count}_{binX}.$$

Adjusted frequency was calculated per mutant per replicate as follows:

$$Q_{mut} = \frac{T_{mut}}{\Sigma_{x=0}^{2} \text{cell count}_{binX}}.$$

An adjusted frequency cutoff of 0.00002 was applied to remove low-frequency reads. Only mutants that have an adjusted frequency of at least 0.00002 in both replicates for all three S2 antibodies were considered.

The occurrence frequency was then calculated as the mean of all six adjusted frequencies:

$$Y_{mut} = \frac{1}{6}\left(Q_{mut,rep1}^{COVA1-07} + Q_{mut,rep2}^{COVA1-07} + Q_{mut,rep1}^{COVA2-14} + Q_{mut,rep2}^{COVA2-14} + Q_{mut,rep1}^{COVA2-18} + Q_{mut,rep2}^{COVA2-18}\right).$$

For each replicate, the binding score of each mutant (B_{mut}) was calculated using:

$$B_{mut} = \frac{\left(\Sigma_{X=0}^{2} F_{mut,binX} \times \text{cell count}_{binX} \times MFI_{binX}\right)}{\Sigma_{x=0}^{2} F_{mut,binX} \times \text{cell count}_{binX}}.$$

Cell counts for bin0 (low expression), bin1 (WT-like expression), and bin2 (high expression) had a ratio of approximately 100:10:1 based on *SI Appendix*, Table S1. As a result, cell $count_{bin0}$, cell $count_{bin1}$, and cell $count_{bin2}$ were set as 100, 10, and 1, respectively. Similarly, the MFI for bin0, bin1, and bin2 had a ratio of approximately 1:50:500. Therefore, MFI_{bin0}, MFI_{bin1}, and MFI_{bin2} were set as 1, 50, and 500, respectively, based on *SI Appendix*, Fig. S1. Subsequently, the binding score of all mutants was scaled to obtain the adjusted binding score (B_{mut}^{adj}) such that the means of adjusted binding scores of nonsense mutations and silent mutations equal 0 and 1, respectively, using the following equation:

$$B_{mut}^{adj} = \frac{B_{mut} - \overline{B_{nonsense}}}{\overline{B_{silient}} - \overline{B_{nonsense}}},$$

where $\overline{B_{nonsense}}$ and $\overline{B_{silient}}$ correspond to the means of nonadjusted binding scores of nonsense mutations and silent mutations, respectively.

Data were plotted in RStudio to visualize binding versus expression. Individual data points were sized according to occurrence frequency, Y_{mut}, as described above.

Flow Cytometry. To validate and quantify surface expression of WT S and its mutants, flow cytometry was performed. First, 4×10^6 HEK293T cells were seeded on wells of six-well plates and incubated overnight at 37 °C. Then, cells were transfected with 2 μg of plasmid encoding WT S or the indicated mutant using Lipofectamine 2000 (Invitrogen) following the manufacturer's protocol. At 20 h posttransfection, cells were harvested and resuspended in ice-cold FACS buffer [2% v/v FBS, 50 mM EDTA in DMEM supplemented with high glucose, L-glutamine and HEPES, without phenol red (Gibco)]. Cells were incubated with 5 μg/mL of RBD antibody CC12.3 (26) for 1 h at 4 °C with gentle rocking. Then, cells were washed once, and resuspended with ice-cold FACS buffer. Cells were incubated with 2 μg/mL of phycoerythrin (PE) anti-human IgG Fc (Clone M1310G05, BioLegend). Cells were washed once, resuspended in ice-cold FACS buffer, and filtered through a 40 μm strainer. Subsequently, cells were analyzed using an Accuri C6 flow cytometer (BD Biosciences). Gating strategy is shown in *SI Appendix*, Fig. S3.

Binding of WT or mutant S to the S2 HR1 public antibodies was validated and quantified via flow cytometry. The same protocol was followed as above except that cells were incubated with 3 μg/mL of COVA1-07, 3 μg/mL of COVA2-14, or 10 μg/mL of COVA2-18. The concentrations of these antibodies were determined via titration using HEK293T landing pad cells stably expressing WT S on their surface. MFI values were calculated by plotting data in FCS Express 6 software (De Novo Software). Fold change in MFI was calculated using the following equation:

$$\text{Fold change in MFI} = \frac{MFI_{mutant} - MFI_{untransfected}}{MFI_{WT} - MFI_{untransfected}}.$$

In Vivo Virus Challenge. Female BALB/c mice that were 8 to 10 wk old were used in this study. Mice were anesthetized with ketamine–xylazine and infected intranasally with 5,000 PFU of the nonrecombinant virus in 50 μL of Dulbecco's Modified Eagle Medium (DMEM) (Gibco). For antibody treatment, mice were injected with 200 μg of antibody (CR9114, COVA1-07, COVA2-14, COVA2-18 WT, COVA2-18 LALA-PG) diluted in 200 μL of PBS through the intravenous route one day before infection. All work with SARS-CoV-2 was performed in the University of Iowa's Biosafety Level 3 (BSL3) laboratories. All animal studies were approved by the University of Iowa Animal Care and Use Committee and meet stipulations of the Guide for the Care and Use of Laboratory Animals.

Histopathology. First, 8 to 10-wk-old female BALB/c mice were intravenously injected with 200 μg of CR9114 or COVA2-18 WT. The next day, mice were anesthetized with ketamine–xylazine and infected intranasally with 5,000 PFU of nonrecombinant virus. Then, 4 d postinfection, mice were killed, and lungs were harvested for virus quantification using the plaque assay. Lung sections were obtained and stained with hematoxylin and eosin. Additionally, pulmonary edema was scored on a scale from 0 to 5, with 0 showing no edema and 5 indicating severe edema.

Statistics. All indicated statistical tests were performed using R or GraphPad Prism 9.

Data, Materials, and Software Availability. Raw reads from deep sequencing data can be accessed at BioProject accession PRJNA888135 (47). Custom code to

analyze deep sequencing data for escape mutations is available at https://github.com/nicwulab/SARS2_HR1_DMS_Abs (48).

ACKNOWLEDGMENTS. We thank the Roy J. Carver Biotechnology Center at the University of Illinois Urbana-Champaign for assistance with fluorescence-activated cell sorting and performing deep sequencing, and Meng Yuan for helpful discussion. This work was supported by NIH R00 AI170996 (L.-Y.R.W.), R01 AI165475 (N.C.W.), and the Searle Scholars Program (N.C.W.).

Author affiliations: [a]Center for Biophysics and Quantitative Biology, University of Illinois Urbana-Champaign, Urbana, IL 61801; [b]Department of Microbiology and Immunology, University of Iowa, Iowa City, IA 52242; [c]Department of Biochemistry, University of Illinois Urbana-Champaign, Urbana, IL 61801; [d]Department of Pathology, University of Iowa, Iowa City, IA 52242; [e]Department of Pathology, Case Western Reserve University School of Medicine, Cleveland, OH 44106; [f]Department of Pediatrics, University of Iowa, Iowa City, IA 52242; [g]Center for Virus-Host-Innate Immunity, Rutgers New Jersey Medical School, Newark, NJ 07103; [h]Department of Microbiology, Biochemistry and Molecular Genetics, Rutgers New Jersey Medical School, Newark, NJ 07103; [i]Carl R. Woese Institute for Genomic Biology, University of Illinois Urbana-Champaign, Urbana, IL 61801; and [j]Carle Illinois College of Medicine, University of Illinois Urbana-Champaign, Urbana, IL 61801

1. A. M. Carabelli *et al.*, SARS-CoV-2 variant biology: Immune escape, transmission and fitness. *Nat. Rev. Microbiol.* **21**, 162–177 (2023).
2. C. B. Jackson, M. Farzan, B. Chen, H. Choe, Mechanisms of SARS-CoV-2 entry into cells. *Nat. Rev. Mol. Cell Biol.* **23**, 3–20 (2022).
3. H. Liu, I. A. Wilson, Protective neutralizing epitopes in SARS-CoV-2. *Immunol. Rev.* **310**, 76–92 (2022).
4. L. Premkumar *et al.*, The receptor binding domain of the viral spike protein is an immunodominant and highly specific target of antibodies in SARS-CoV-2 patients. *Sci. Immunol.* **5**, eabc8413 (2020).
5. M. Yuan, H. Liu, N. C. Wu, I. A. Wilson, Recognition of the SARS-CoV-2 receptor binding domain by neutralizing antibodies. *Biochem. Biophys. Res. Commun.* **538**, 192–203 (2021).
6. T. P. Peacock *et al.*, The altered entry pathway and antigenic distance of the SARS-CoV-2 Omicron variant map to separate domains of spike protein. bioRxiv [Preprint] (2022). https://doi.org/10.1101/2021.12.31.474653 (Accessed 19 September 2023).
7. C. Sun *et al.*, Mutation N856K in spike reduces fusogenicity and infectivity of Omicron BA.1. *Signal Transduct. Target Ther.* **8**, 75 (2023).
8. Z. Cui *et al.*, Structural and functional characterizations of infectivity and immune evasion of SARS-CoV-2 Omicron. *Cell* **185**, 860–871.e13 (2022).
9. C. Dacon *et al.*, Broadly neutralizing antibodies target the coronavirus fusion peptide. *Science* **377**, 728–735 (2022).
10. X. Sun *et al.*, Neutralization mechanism of a human antibody with pan-coronavirus reactivity including SARS-CoV-2. *Nat. Microbiol.* **7**, 1063–1074 (2022).
11. J. S. Low *et al.*, ACE2-binding exposes the SARS-CoV-2 fusion peptide to broadly neutralizing coronavirus antibodies. *Science* **377**, 735–742 (2022).
12. F. Bianchini *et al.*, Human neutralizing antibodies to cold linear epitopes and subdomain 1 of the SARS-CoV-2 spike glycoprotein. *Sci. Immunol.* **8**, eade0958 (2023).
13. P. Zhou *et al.*, Broadly neutralizing anti-S2 antibodies protect against all three human betacoronaviruses that cause deadly disease. *Immunity* **56**, 669–686.e7 (2023).
14. D. Pinto *et al.*, Broad betacoronavirus neutralization by a stem helix-specific human antibody. *Science* **373**, 1109–1116 (2021).
15. W. Li *et al.*, Structural basis and mode of action for two broadly neutralizing antibodies against SARS-CoV-2 emerging variants of concern. *Cell Rep.* **38**, 110210 (2022).
16. C. Wang *et al.*, A conserved immunogenic and vulnerable site on the coronavirus spike protein delineated by cross-reactive monoclonal antibodies. *Nat. Commun.* **12**, 1715 (2021).
17. C. Dacon *et al.*, Rare, convergent antibodies targeting the stem helix broadly neutralize diverse betacoronaviruses. *Cell Host Microbe* **31**, 97–111.e112 (2023).
18. M. Claireaux *et al.*, A public antibody class recognizes an S2 epitope exposed on open conformations of SARS-CoV-2 spike. *Nat. Commun.* **13**, 4539 (2022).
19. E. C. Chen *et al.*, Convergent antibody responses to the SARS-CoV-2 spike protein in convalescent and vaccinated individuals. *Cell Rep.* **36**, 109604 (2021).
20. M. Sakharkar *et al.*, Prolonged evolution of the human B cell response to SARS-CoV-2 infection. *Sci. Immunol.* **6**, eabg6916 (2021).
21. F. Amanat *et al.*, SARS-CoV-2 mRNA vaccination induces functionally diverse antibodies to NTD, RBD, and S2. *Cell* **184**, 3936–3948.e10 (2021).
22. L. R. Wong *et al.*, Eicosanoid signalling blockade protects middle-aged mice from severe COVID-19. *Nature* **605**, 146–151 (2022).
23. C. Dreyfus *et al.*, Highly conserved protective epitopes on influenza B viruses. *Science* **337**, 1343–1348 (2012).
24. M. Lo *et al.*, Effector-attenuating substitutions that maintain antibody stability and reduce toxicity in mice. *J. Biol. Chem.* **292**, 3900–3908 (2017).
25. T. J. C. Tan *et al.*, High-throughput identification of prefusion-stabilizing mutations in SARS-CoV-2 spike. *Nat. Commun.* **14**, 2003 (2023).
26. M. Yuan *et al.*, Structural basis of a shared antibody response to SARS-CoV-2. *Science* **369**, 1119–1123 (2020).
27. Y. Shu, J. McCauley, GISAID: Global initiative on sharing all influenza data – from vision to reality. *Euro Surveill* **22**, 30494 (2017).
28. A. C. Walls *et al.*, Structure, function, and antigenicity of the SARS-CoV-2 spike glycoprotein. *Cell* **181**, 281–292.e6 (2020).
29. Y. Furusawa *et al.*, In SARS-CoV-2 delta variants, Spike-P681R and D950N promote membrane fusion, Spike-P681R enhances spike cleavage, but neither substitution affects pathogenicity in hamsters. *eBioMedicine* **91**, 104561 (2023).
30. S. B. Park *et al.*, SARS-CoV-2 omicron variants harbor spike protein mutations responsible for their attenuated fusogenic phenotype. *Commun. Biol.* **6**, 556 (2023).
31. M. G. Joyce *et al.*, Vaccine-induced antibodies that neutralize group 1 and group 2 influenza A viruses. *Cell* **166**, 609–623 (2016).
32. I. Setliff *et al.*, Multi-donor longitudinal antibody repertoire sequencing reveals the existence of public antibody clonotypes in HIV-1 infection. *Cell Host Microbe* **23**, 845–854.e6 (2018).
33. Y. Wang *et al.*, A large-scale systematic survey reveals recurring molecular features of public antibody responses to SARS-CoV-2. *Immunity* **55**, 1105–1117.e4 (2022).
34. T. J. C. Tan *et al.*, Sequence signatures of two public antibody clonotypes that bind SARS-CoV-2 receptor binding domain. *Nat. Commun.* **12**, 3815 (2021).
35. Q. Zhang *et al.*, Potent and protective IGHV3-53/3-66 public antibodies and their shared escape mutant on the spike of SARS-CoV-2. *Nat. Commun.* **12**, 4210 (2021).
36. M. Yuan *et al.*, Structural and functional ramifications of antigenic drift in recent SARS-CoV-2 variants. *Science* **373**, 818–823 (2021).
37. G. Shi *et al.*, Omicron Spike confers enhanced infectivity and interferon resistance to SARS-CoV-2 in human nasal tissue. *Nat. Commun.* **15**, 889 (2024).
38. Y. Wang *et al.*, Conformational dynamics of the Beta and Kappa SARS-CoV-2 spike proteins and their complexes with ACE2 receptor revealed by cryo-EM. *Nat. Commun.* **12**, 7345 (2021).
39. Z. Zhao *et al.*, Omicron SARS-CoV-2 mutations stabilize spike up-RBD conformation and lead to a non-RBM-binding monoclonal antibody escape. *Nat. Commun.* **13**, 4958 (2022).
40. D. M. Morens, J. K. Taubenberger, A. S. Fauci, Universal coronavirus vaccines–An urgent need. *N. Engl. J. Med.* **386**, 297–299 (2022).
41. S. A. Kemp *et al.*, SARS-CoV-2 evolution during treatment of chronic infection. *Nature* **592**, 277–282 (2021).
42. B. Dadonaite *et al.*, A pseudovirus system enables deep mutational scanning of the full SARS-CoV-2 spike. *Cell* **186**, 1263–1278.e20 (2023).
43. K. W. Ng *et al.*, SARS-CoV-2 S2-targeted vaccination elicits broadly neutralizing antibodies. *Sci. Transl. Med.* **14**, eabn3715 (2022).
44. W. Pang *et al.*, A variant-proof SARS-CoV-2 vaccine targeting HR1 domain in S2 subunit of spike protein. *Cell Res.* **32**, 1068–1085 (2022).
45. P. J. Halfmann *et al.*, Multivalent S2-based vaccines provide broad protection against SARS-CoV-2 variants of concern and pangolin coronaviruses. *eBioMedicine* **86**, 104341 (2022).
46. J. Zhang, K. Kobert, T. Flouri, A. Stamatakis, PEAR: A fast and accurate Illumina Paired-End reAd mergeR. *Bioinformatics* **30**, 614–620 (2014).
47. T. J. C. Tan *et al.*, Escape mutations in the core fusion machinery of SARS-CoV-2 spike protein. NCBI SRA. https://www.ncbi.nlm.nih.gov/bioproject?term=PRJNA888135. Deposited 7 October 2022.
48. T. J. C. Tan *et al.*, SARS2_HR1_DMS_Abs. GitHub. https://github.com/nicwulab/SARS2_HR1_DMS_Abs. Deposited 29 September 2023.